J Mater Sci (2021) 56:4366–4379

Energy materials

Fabrication of visible-light-response face-contact $ZnSnO_3$@g-C_3N_4 core–shell heterojunction for highly efficient photocatalytic degradation of tetracycline contaminant and mechanism insight

Xiufeng Zhu[1], Feng Guo[1,*], Jingjing Pan[1], Haoran Sun[1], Lingling Gao[1], Jingxiao Deng[1], Xunyi Zhu[1], and Weilong Shi[2,*]

[1] *School of Energy and Power, Jiangsu University of Science and Technology, Zhenjiang 212003, Jiangsu, People's Republic of China*
[2] *School of Material Science and Engineering, Jiangsu University of Science and Technology, Zhenjiang 212003, People's Republic of China*

Received: 13 August 2020
Accepted: 4 November 2020
Published online:
16 November 2020

ABSTRACT

The large-scale consumption and discharge of antibiotic tetracycline (TC) urge us to search for a highly efficient and eco-friendly technology to remove it. In this work, face-contact $ZnSnO_3$@g-C_3N_4 core–shell heterojunction was successfully constructed via one-step calcination route. The experimental data indicate that the photocatalytic TC removal performance of $ZnSnO_3$@g-C_3N_4 (1:3) reaches 90.8% within 120 min under the same condition compared with bulk g-C_3N_4 (32% degradation) and $ZnSnO_3$ (9% degradation). The improved photocatalytic activity is ascribed to the formation of core–shell structure between $ZnSnO_3$ and g-C_3N_4 which not only enlarges visible light response but also effectively separates electron–hole pairs. Meanwhile, this face-contact ZSO-CN photocatalyst displays much more contact interfaces than the point-contact ZSO-CN photocatalyst, and the contact interfaces could play the part of efficient channels for charge transfer. Finally, the photocatalytic reaction mechanism on $ZnSnO_3$@g-C_3N_4 was also stated at length through active species capture and electron spin resonance (ESR) tests. And the possible intermediates products were discussed through the liquid chromatography–mass spectrometry (LC–MS) analysis.

Handling Editor: Joshua Tong.

Address correspondence to E-mail: gfeng0105@126.com; shiwl@just.edu.cn

https://doi.org/10.1007/s10853-020-05542-1

Introduction

With the abuse of antibiotics, the random disposal of drug waste and the wanton discharge of drug wastewater, the purification of wastewater containing antibiotics has become a problem of human concern [1]. Semiconductors-based photocatalysis is considered as a promising and effective technology to remove organic contaminants in the aqueous solution because of its simple equipment and easy control without secondary pollution [2–11]. Up to the present, various metal oxide semiconductors have been developed as photocatalysts, such as TiO_2, ZnO, SnO_2, Bi_2O_3, $BiVO_4$ and $ZnSnO_3$ [12–16]. Among them, $ZnSnO_3$ has attracted great interest in the photocatalytic field due to its high electron mobility, fast electrical conductivity and strong negative reduction potential of excited electrons [17, 18]. However, like most wide-band-gap semiconductors, $ZnSnO_3$ cannot be excited to generate photogenerated carriers in the visible region, which leads to practical limitation [19].

Considerable research efforts have been devoted to expanding the photocatalytic activity of $ZnSnO_3$ in the range of visible light, which include doping elements to broaden the visible light absorbance [20] and carbon-based material sensitization to enhance the visible-light-response range [21]. Besides, coupling the $ZnSnO_3$ with the visible-light-driven semiconductors to form heterojunctions is also an advisable strategy [22]. Recently, graphitic carbon nitride (g-C_3N_4) has been attracted much attention because of its relatively narrow band gap, low cost, high chemical stability and innocuity [23–27]. In recent years, many reports of employing g-C_3N_4 to improve the photocatalytic performance of wide-band-gap semiconductors have been published. For example, Tan et al. modified the TiO_2 with g-C_3N_4, which expands the light absorption of the photocatalysts and exhibits the favorable photocatalytic H_2 evolution efficiency under visible light [28]. Tang's group synthesized g-C_3N_4/ZnO and displayed the excellent visible light photodegradable efficiency by degrading 94% of Rhodamine B (RhB) in two hours, which is mainly caused by the heterostructure between g-C_3N_4 and ZnO; the photoexcited electrons in CB of g-C_3N_4 can be transferred into the CB of ZnO, thus effectively separating electrons and holes [29]. Zhang et al. fabricated visible-light-response $Bi_2O_2CO_3$/g-C_3N_4 heterojunction photocatalysts which showed greatly improved activity for removing the three model pollutants of CH_3CHO, RhB and Cr (VI) [30]. Concerning the research on g-C_3N_4/$ZnSnO_3$ composite, Chen's group has utilized zero-dimensional (0D) $ZnSnO_3$ nanoparticles to coat on the surface of two-dimensional (2D) g-C_3N_4 nanosheets forming the g-C_3N_4/$ZnSnO_3$ heterojunction to effectively enhance its photocatalytic activity under visible light irradiation [31]. However, with respect to the contact area at the interface of the heterojunction, the reactive sites of this point contact formed by 0D/2D heterojunction are often less than that of the face-contact heterojunction [32]. Thus, in order to further enhance the photocatalytic activity, the construction of g-C_3N_4/$ZnSnO_3$ heterojunction with face-contact is more reasonable.

As is known, to design and develop the core–shell structure could provide more channels for charge transport and more surface reactive sites. For example, Hou et al. prepared $BiVO_4$@TiO_2 core–shell hybrid mesoporous nanofibers for photocatalytic hydrogen production, exhibiting the superior photocatalytic H_2 production efficiency benefiting from the high specific surface area with increased reaction sites [33]. Meanwhile, Liu's group prepared the $Cd_2Ge_2O_6$/CdS core–shell structure photocatalysts, which significantly improve the charge migration capability due to the large-area contact of core–shell structure [34]. In addition, the construction of core–shell structure can also improve the stability of the core material by covering with a stable shell material. An et al. prepared the core–shell Ag_2CO_3@g-C_3N_4 photocatalyst, aiming at the prevention of the photocorrosion of Ag_2CO_3 through the outer g-C_3N_4 shell in the composite [35]. Similarly, Jia et al. reported hybrid core–shell microgels with Cu_2O nanocubes as the core and thermosensitive PNIPAM as the shell, which presents excellent colloidal stability [36]. Consequently, systematic design and controllable prepared g-C_3N_4/$ZnSnO_3$ with core–shell nanostructure is expected to achieve the high active visible-light-driven heterojunction photocatalyst.

In this work, face-contact $ZnSnO_3$@g-C_3N_4 core–shell heterojunction was successfully constructed via the calcination route. This composite photocatalyst is used for degrading TC under visible light irradiation ($\lambda > 420$ nm). It not only expands the absorption of visible light but also effectively separates the electrons and holes; thus, the photocatalytic degradation

performance of TC is greatly improved. Moreover, the possible degradation mechanism over $ZnSnO_3$@g-C_3N_4 was investigated through active species capture and electron spin resonance (ESR) experiments.

Experimental section

Synthesis of g-C_3N_4

Typically, 2 g melamine was in a covered crucible heated to 550 °C maintained for 3 h with a ramp speed of 5 °C/min. After cooling to room temperature, the resulting solids were ground to obtain the g-C_3N_4 powder.

Synthesis of $ZnSn(OH)_6$ cubes

$ZnSn(OH)_6$ cubes were prepared using a typical synthetic method according to the previous report [16]. First, 0.158 g of $SnCl_4{\cdot}5H_2O$ was dissolved in 20 mL of deionized water and stirred at room temperature. The pH of the mixed solution was adjusted to 12.0 by adding NaOH solution, and 0.1295 g of $ZnSO_4{\cdot}7H_2O$ was added under stirring at 60 °C until the appearance of a white precipitate. It was then aged at 60 °C for 12 h, cooled to room temperature and washed six times with distilled water and absolute ethanol to remove residual ions. Finally, the white precipitate was dried at 60 °C to obtain $ZnSn(OH)_6$ cubes powder.

Synthesis of $ZnSnO_3$@g-C_3N_4

The synthetic process of $ZnSnO_3$@g-C_3N_4 is shown in Scheme 1. Briefly, 200 mg of $ZnSn(OH)_6$ cubes was immersed in 20 mL deionized water, and then a certain mass of cyanamide solution (50% aqueous solution) was added. Next, the mixed solution was sonicated at 60 °C for 2 h and stirred for 12 h. It was then centrifuged, dried and calcined at 580 °C for 2 h. The obtained $ZnSnO_3$@g-C_3N_4 samples were expressed as ZSO@CN (X), where X refers to the mass ratio of $ZnSn(OH)_6$ and cyanamide. The pure $ZnSnO_3$ sample was fabricated under the same conditions in the absence of cyanamide and labeled as ZSO.

The characterizations and photocatalytic experiments can be listed in the Supporting Information.

Results and discussion

The morphologies of ZSO and ZSO@CN (1:3) were observed by scanning electron microscope (SEM) and transmission electron microscope (TEM). From the SEM image of ZSO (Fig. 1a), it can be seen that the ZSO possesses a cube-like morphology with smooth surfaces and the average size of around 200 nm. After introducing the CN, the morphology of ZSO@CN composite is hardly changed in comparison with pure ZSO (Fig. 1b). And the specific morphologies of the synthesized samples were further employed by the TEM measurement. As can be seen in Fig. 1c, d, the lattice spacing on the crystal we measured is 0.262 nm, which corresponds to the (110) plane of $ZnSnO_3$ nanocubes [37]. Notably, for the ZSO@CN composite, the layer of CN is coated on the outer surface of nanocube-like ZSO material, which is approximately 4.0 nm (Fig. 1e, f) to form a distinct core–shell structure.

To estimate the distribution of the elements in the ZSO@CN composite, the HAADF-SEM and elements mapping were carried out. As shown in Fig. 2a–f, the HAADF-SEM and C, N, Zn, Sn and O elements are detected and all the elements are continuous and concentrating distribution, unambiguously

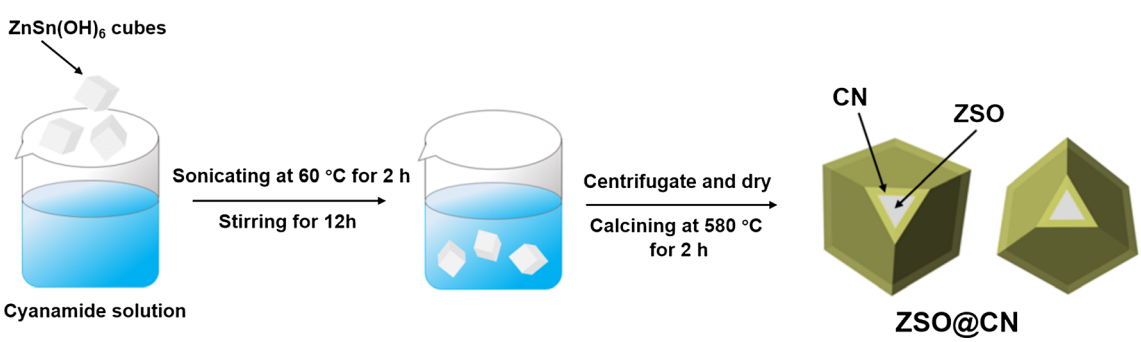

Scheme 1 Schematic illustration of the fabrication process over the ZSO@CN core–shell composite photocatalyst.

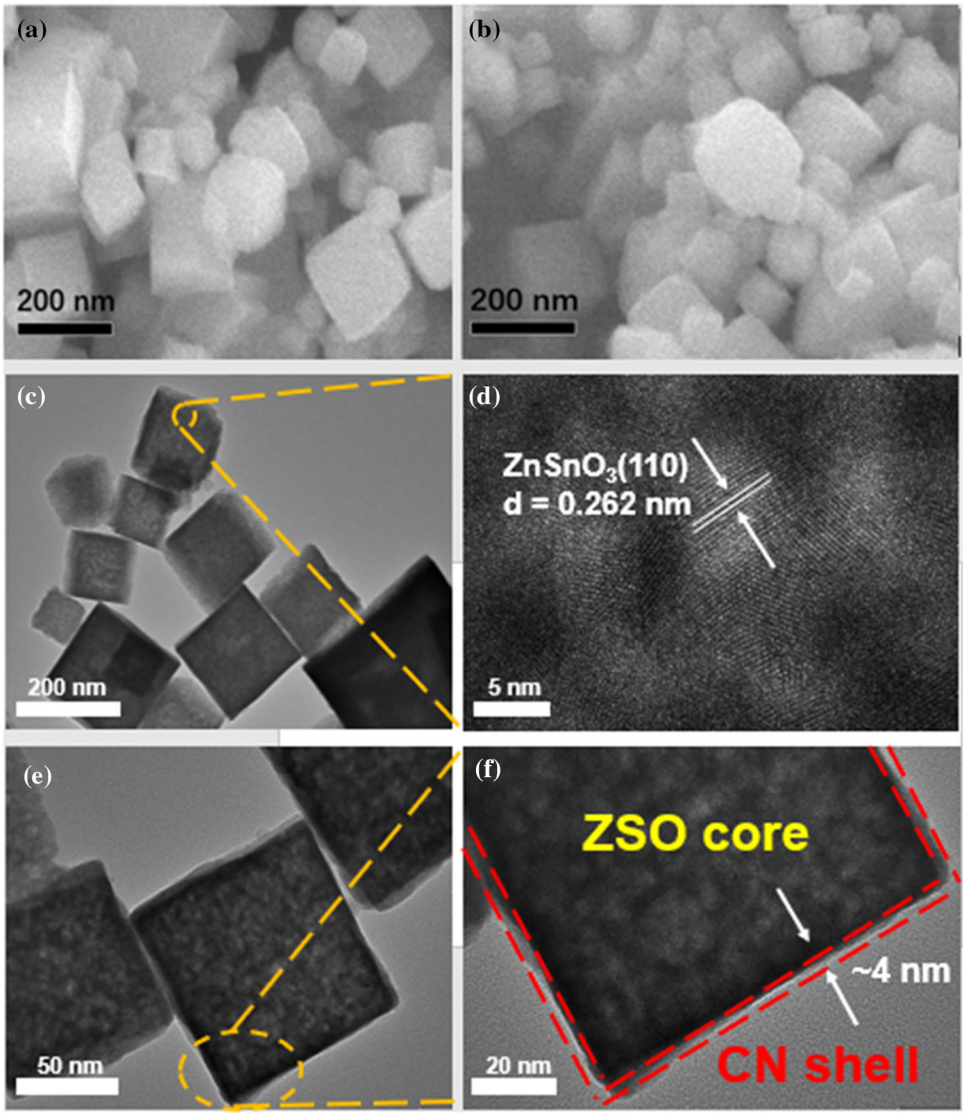

Figure 1 SEM images of **a** ZSO and **b** ZSO@CN (1:3). TEM and HRTEM images of **c**, **d** ZSO and **e**, **f** ZSO@CN (1:3).

identifying that CN has been successfully coated on the outer surface of ZSO cubic nanostructure, although the C and N elements in the elements mapping are not obvious due to the low content of CN on the outer surface.

In Fig. 3, X-ray diffraction (XRD) patterns of CN, ZSO and ZSO@CN (1:3) were recorded. It is observed that there are two characteristic diffraction peaks at (002) and (100) planes in the XRD pattern of CN, which were ascribed to in-plane structural packing motifs and the interlayer accumulation of aromatic system [38]. For the porous ZSO cubes, the characteristic diffraction peaks are assigned to the (012), (110) and (116) planes, respectively [39]. The XRD pattern of as-prepared ZSO@CN (1:3) sample almost shows the typical peaks of ZSO. However, the characteristic peaks of CN shell could not be observed in the XRD pattern of ZSO@CN (1:3) sample, which is due to the shell thickness that belongs to a short-range ordered structure and the limited amount and low intensity of CN [40].

As illustrated in Fig. 4, the Fourier transform infrared (FT-IR) spectra of ZSO, pure CN and ZSO@CN (1:3) samples are adopted. From the spectra of CN, several peaks between 1230 and 1650 cm^{-1} are observed, which ascribe to the aromatic C–N stretching and C=N stretching vibration modes [41]. The other two peaks about 808 and 3200–3400 cm^{-1} are observed separately in the spectra: The 808 cm^{-1} can be attributed to the breathing mode of triazine unit, whereas the 3200–3400 cm^{-1} to the stretching vibration of N–H [42]. For pristine ZSO, the peaks

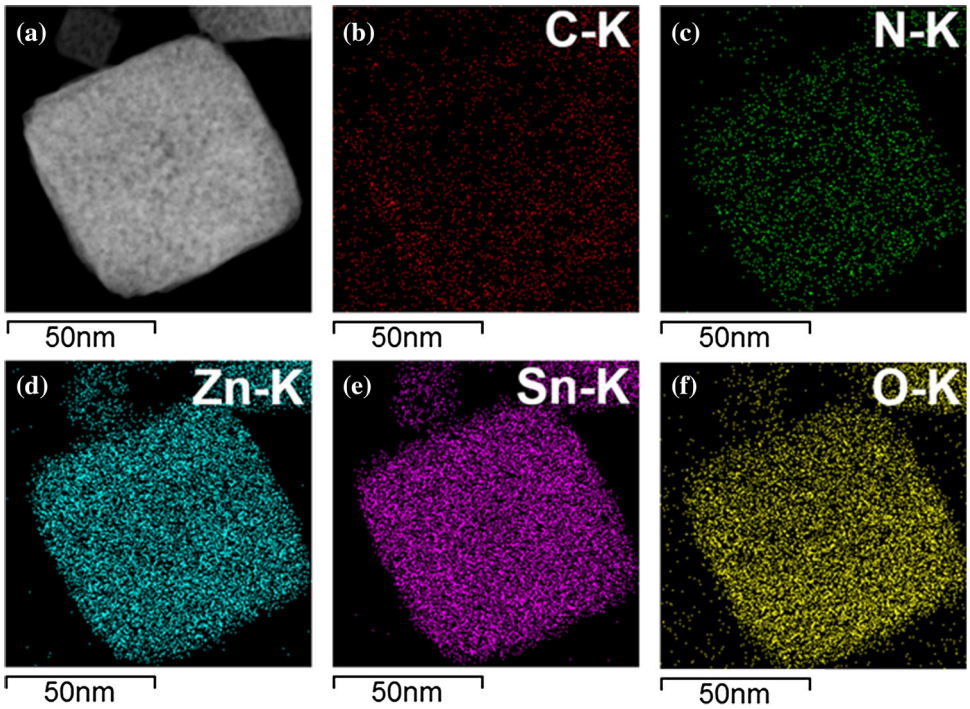

Figure 2 **a** HAADF-SEM and **b–f** elemental mapping images of ZSO@CN (1:3).

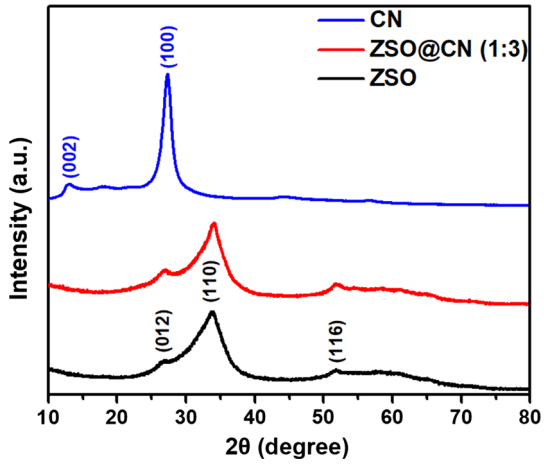

Figure 3 XRD patterns of CN, ZSO and ZSO@CN (1:3).

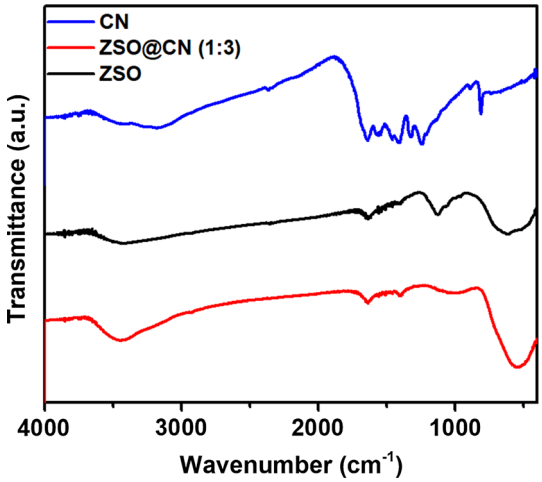

Figure 4 FT-IR spectra of CN, ZSO and ZSO@CN (1:3).

located at 475 and 600 cm^{-1} can be attributed to the vibration modes of Zn–O and Sn–O [43]. Similar to the XRD results, the main characteristic peaks of ZSO@CN (1:3) are basically consistent with ZSO in the FT-IR spectra. In the ZSO@CN (1:3) core–shell composite photocatalyst, it is difficult to observe the main characteristic peaks of CN, which is due to the low content of CN in the ZSO@CN (1:3).

X-ray photoelectron spectroscopy (XPS) technique was performed for confirming the chemical valences and compositions of CN, ZSO and ZSO@CN (1:3), and the corresponding spectra are displayed in Fig. 5.

Figure 5a shows two main elements (C and N) in the survey spectrum of CN and three main elements (Zn, Sn and O) in the survey spectrum of ZSO, respectively. However, there are no obvious diffraction peaks representing C and N elements in the survey spectrum of ZSO@CN, which is due to the little content of CN in ZSO@CN, but reflected the peak intensities of the C 1 s and N 1 s high-resolution XPS spectra. There are two obvious diffraction peaks located at 288.2 eV and 284.6 eV in the high-resolution XPS spectrum of C 1 s for CN (Fig. 5b), which belongs to sp^2 C–C bonds and sp^2-bonded carbon (N–

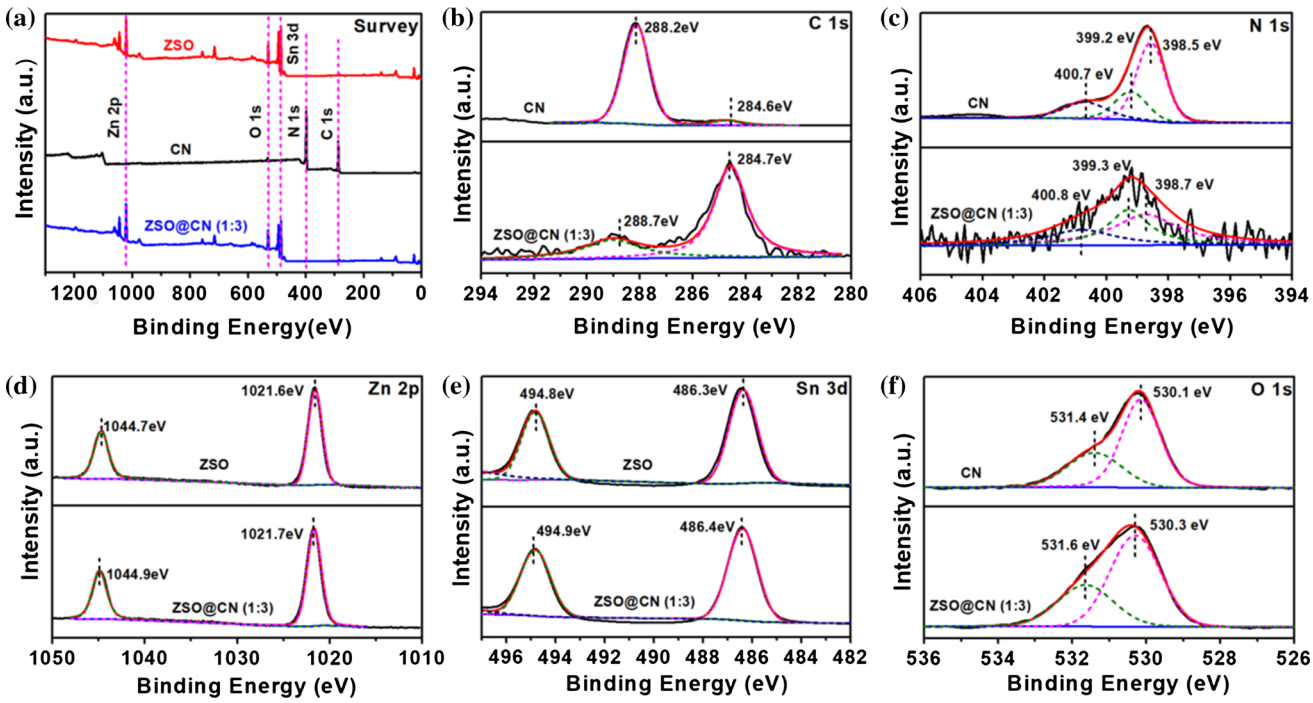

Figure 5 **a** Survey XPS spectra of CN, ZSO and ZSO@CN (1:3). High-resolution XPS spectra of **b** C 1 s, **c** N 1 s, **d** Zn 2p, **e** Sn 3d and **f** O 1 s.

C=N), respectively [44]. The N 1 s spectrum of CN (Fig. 5c) can be decomposed into three peaks located at 398.5, 399.2 and 400.7 eV, which are corresponded to C–N–C, N–$(C)_3$ and N–H, respectively [29]. The Zn 2p spectrum of ZSO (Fig. 5d) should be deconvoluted by two peaks at 1021.6 and 1044.7 eV which are associated with Zn $2p_{3/2}$ and Zn $2p_{1/2}$. In the Sn 3d spectrum of ZSO (Fig. 5e), the peaks appear at 486.3 eV for Sn $3d_{3/2}$ and 494.8 eV for Sn $3d_{5/2}$, respectively. The O 1 s spectra of ZSO (Fig. 5f) centered at 530.1 and 531.4 eV are attributed to the metal oxide bonds and –OH groups, respectively [45]. From the high-resolution XPS spectra of ZSO@CN (1:3), the positive shifts of five elements are seen, which are due to the heterojunction formed successfully.

In order to study the optical properties of as-prepared photocatalysts, the UV–Vis diffuse reflectance spectra of CN, ZSO and ZSO@CN (1:3) samples are measured and displayed in Fig. 6a. It can be seen that pristine CN shows an obvious absorption edge at around 478 nm, and in the visible light range of 400–800 nm pure ZSO shows a weak absorption. When coupling ZSO core with CN shell, the absorption capacity of ZSO@CN (1:3) composite photocatalyst has been enhanced compared with pure phase ZSO, which indicated that the addition of CN could improve the utilization rate of ZSO to light, so it was beneficial to the improvement in photocatalytic performance. According to the Tauc formula, the band gap values of ZSO and CN can be calculated to be 3.25 and 2.73 eV (Fig. 6b), respectively.

The visible-light-driven photocatalytic performance of the prepared photocatalysts was tested by the degradation of TC solution. Before the photocatalytic experiment, in the dark for 30 min, all the samples reached the adsorption equilibrium. The photocatalytic test results (Fig. 7a) reveal that compared to individual CN (32% degradation) and ZSO (9% degradation) within the same irradiation time, the ZSO@CN core–shell composite photocatalysts owned the superior photocatalytic activity. Notably, the photocatalytic activity of the ZSO@CN core–shell structure depends on the quality of CN introduction. With the increase in CN mass content (from 1:0.5 to 1:3), the photocatalytic activity of ZSO@CN core–shell structure was enhanced, and ZSO@CN (1:3) exhibited the optimum TC degradation rate of 90.8% after 120-min irradiation. Further increasing the content of CN mass can lead to a decrease in the ZSO@CN core–shell structure. This is attributed to the excessive CN (1:5 and 1:10 in the core–shell structure when the amount of CN is higher than its

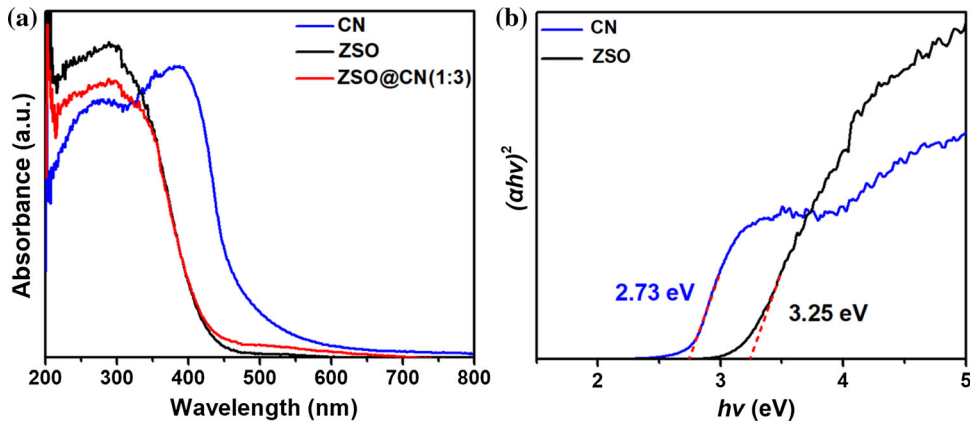

Figure 6 **a** UV–Vis diffuse reflectance spectra of CN, ZSO and ZSO@CN(1:3). **b** Band gap energies of as-prepared pure ZSO and CN.

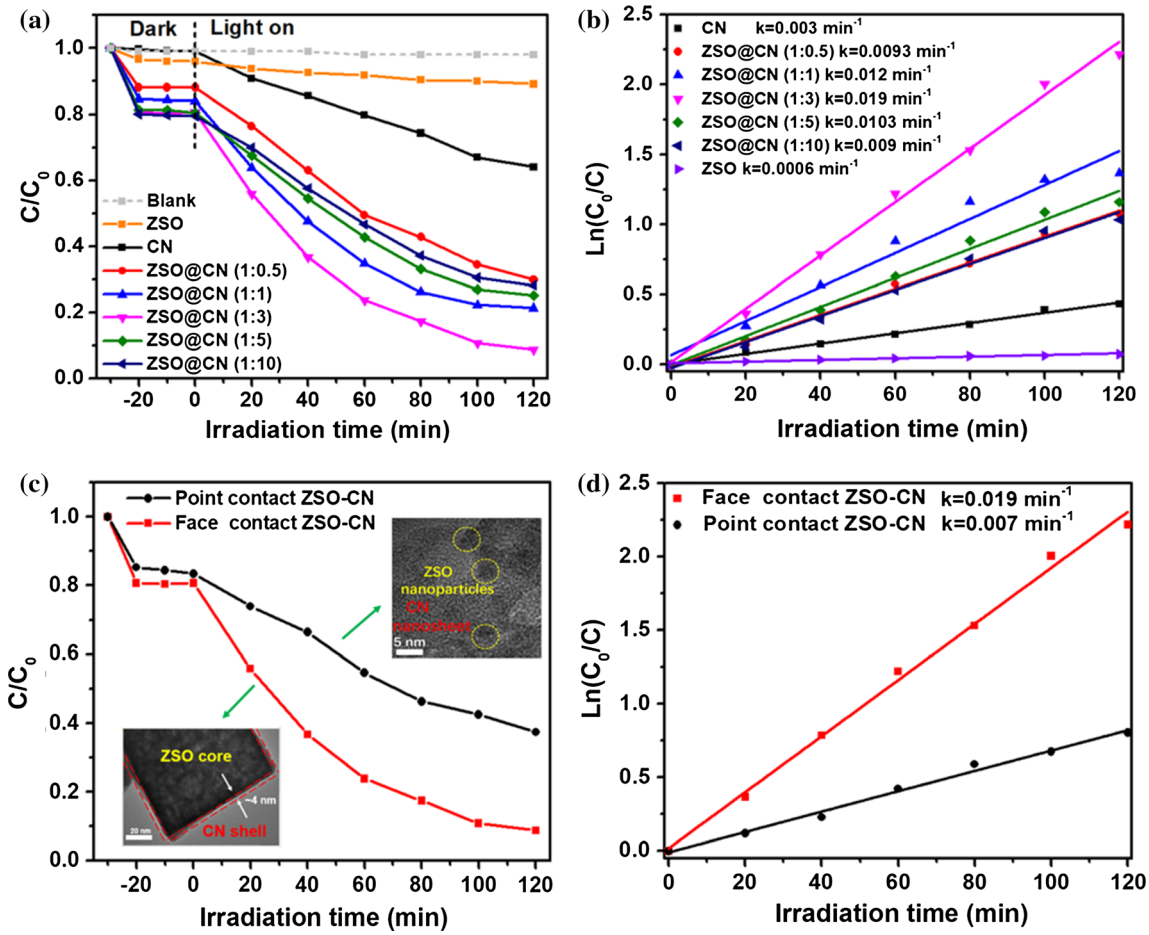

Figure 7 **a** TC degradation over as-prepared photocatalysts under visible light irradiation and **b** the corresponding pseudo-first-order reaction kinetics and rate constants. **c** TC degradation over ZSO-CN composite photocatalysts with different contact modes under visible light irradiation and **d** the corresponding pseudo-first-order reaction kinetics and rate constants.

optimum deposition) which could lead to agglomeration state of the CN surface under such conditions without forming an effective core–shell interface, which hinders the transfer of photogenerated electrons [46]. As shown in Fig. 7b, all prepared photocatalysts follow the pseudo-first-order rule. Based on the calculated k values, the ZSO@CN (1:3) owns the highest TC degradation k value (0.019 min^{-1}), which is around 6.33 and 31.67 times higher than that of CN (0.003 min^{-1}) and ZSO

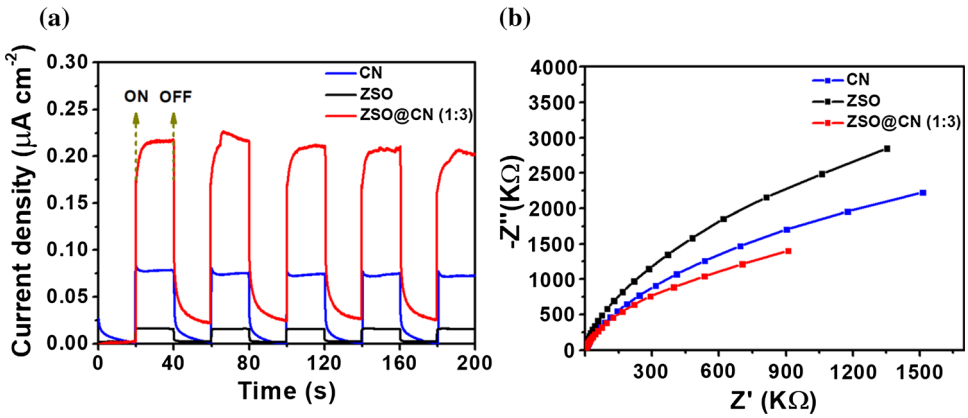

Figure 8 **a** Transient photocurrent spectra and **b** EIS spectra of CN, ZSO and ZSO@CN (1:3).

(0.0006 min^{-1}), respectively. Besides, for exploring the mineralization degree of TC during the photocatalysis, total organic carbon (TOC) removal rate over the ZSO@CN under visible light illumination was tested. As exhibited in Fig.S1, the removal rate of TOC was only 0.5% without photocatalyst, while ZSO@CN (1:3) photocatalyst reduced TOC by 46.2%. The results display that the ZSO@CN composite had good mineralization efficiency for the degradation of TC. In order to further reveal the advantage of the as-prepared photocatalyst with surface contact, we carried out a comparative experiment of ZSO nanoparticles coated on the surface of CN nanosheets to form point-contact ZSO-CN based on previous report [31]. The results of TC degradation and the pseudo-first-order reaction kinetics and *k* values of the as-prepared photocatalysts with different contact modes for TC degradation were further investigated. As displayed in Fig. 7c, it can be seen that the degradation of TC solution of the ZSO-CN with face contact is always higher than that with point contact. From Fig. 7d, the face-contact ZSO-CN shows the higher TC degradation k value (0.019 min^{-1}), which is about 2.71 times higher than that of point-contact ZSO-CN (0.007 min^{-1}). It is obvious that the face-contact ZSO-CN photocatalyst displays much more contact interfaces than the point-contact ZSO-CN photocatalyst, and the contact interfaces could play the part of efficient channels for charge transfer [47], leading to the higher photocatalytic degradation performance of face-contact ZSO-CN composite photocatalyst.

The BET analysis was carried out, and the result is shown in Fig.S2. It can be seen that the specific surface area of ZSO@CN (40.3 $m^2 g^{-1}$) is higher than that of ZSO (35.1 $m^2 g^{-1}$). This result reveals that the increasing specific surface area in ZSO@CN can provide more activity sites and be beneficial to improve the photocatalytic activity. Photocurrent experiments were carried out to reveal the separation and migration properties of photoinduced electron–hole pairs. The results are shown in Fig. 8a. Because of the wide band gap of ZSO, it is hard to use visible light, and the photocurrent intensity of pristine ZSO is very low. Notably, the photocurrent intensity for pure CN is higher than that of ZSO, which is consistent with UV–Vis diffuse reflectance spectra. Evidently, the ZSO@CN (1:3) photocatalyst displayed the highest photocurrent intensity, implying that the core–shell heterostructure between CN and ZSO is beneficial to promote the separation of electrons and holes. Similarly, compared to other samples (Fig. 8b), the impedance arc radius of the ZSO@CN (1:3) photocatalyst was the smallest, which also verified that charge transfer is promoted in the core–shell heterostructure.

Additionally, nanosecond (ns) time-resolved fluorescence decay spectra were recorded to further investigate charge transfer and separation (Fig. 9a). The corresponding parameters are summarized in Table 1; the fluorescence peak decay of ZSO@CN (1:3) (τ_1 = 1.08 ns, τ_2 = 4.82 ns) was shorter than that of the CN with half-lives of τ_1 = 2.05 ns and τ_2 = 6.50 ns. Meanwhile, the corresponding average fluorescence lifetimes (τ_{av}) of CN and ZSO@CN (1:3) are obtained to be 5.21 and 3.22 ns, respectively. The shorter lifetime indicates that the recombination rate of photogenerated charge carriers decreases, which makes the separation efficiency of photoinduced charge higher, according to the previous reports [48]. Hence, the τ_{av} of ZSO@CN (1:3) is shorter than that of CN, which further proves that the interfacial charge transfer can promote charge separation. In order to

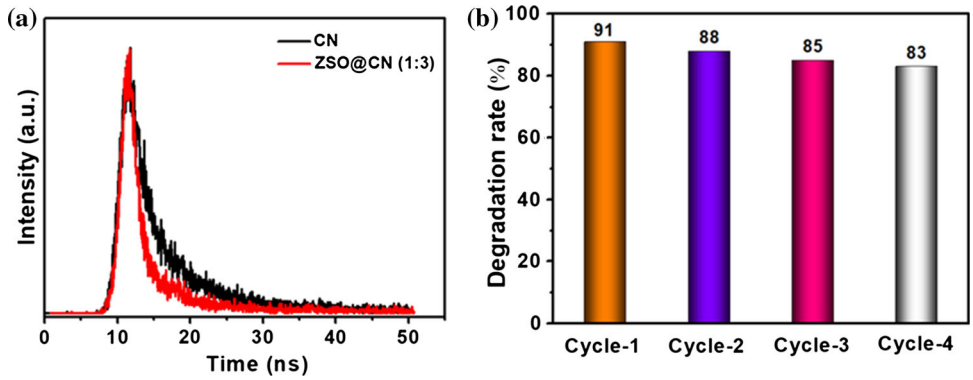

Figure 9 **a** Time-resolved transient PL decay spectra of CN and ZSO@CN (1:3). **b** Cycle stability tests of as-prepared ZSO@CN (1:3) photocatalyst.

Table 1 Fluorescence lifetime parameters summarized from the time-resolved PL spectra with fitting curves

Samples	τ_1 (ns)	A_1(%)	τ_2 (ns)	A_2(%)	τ_{av} (ns)
CN	2.05	28.95	6.50	71.05	5.21
ZSO@CN (1:3)	1.08	42.73	4.82	57.27	3.22

assess the stability of ZSO@CN composite photocatalyst, the recycling experiment was performed and the result is exhibited in Fig. 9b. After four recycles, the photocatalytic degradation rate of TC remained above 83%, revealing that the ZSO@CN (1:3) composite possesses the outstanding photocatalytic stability.

In order to confirm the main active species of ZSO@CN, different scavengers, such as nitrogen (N_2), isopropyl (IPA) and disodium ethylenediamine tetraacetic acid (EDTA), were added into the reaction solution for capturing superoxide radicals ($\cdot O_2^-$), hydroxyl radicals (·OH) and holes (h^+), respectively. As shown in Fig. 10a, the addition of IPA into the reaction system did not significantly inhibit the degradation rate of TC. However, after adding N_2 and EDTA into the reaction system, the photocatalytic degradation rate of ZSO@CN distinctly decreased from 91 to 49% and 33%, respectively. As shown in Fig. 10b, taking ZSO@CN composite under visible light irradiation, electron spin resonance (ESR) test was carried out to further clarify the existence of $\cdot O_2^-$ active substance in the photocatalysis. In the absence of light, there is no obvious peak of $\cdot O_2^-$. Under visible light irradiation, the peak value of the $\cdot O_2^-$ crack of the ZSO@CN composite was significantly enhanced. In summary, as we all know, $\cdot O_2^-$ and h^+ are produced during the photocatalytic process and play the significant roles in the degradation of TC over ZSO@CN core–shell composite photocatalyst.

To further explore the main intermediate products during the photocatalysis over ZSO@CN (1:3) photocatalyst, the liquid chromatography–mass spectrometry (LC–MS) technique was performed and the corresponding spectrum is exhibited in Fig.S3. It is well known that the substance with a molecular weight of 445 is TC [49]. Moreover, m/z values of 410, 388, 337, 241, 201, 154 and 141 were also formed in the degradation process, which were labeled as TC_2–TC8, respectively, and the possible degradation

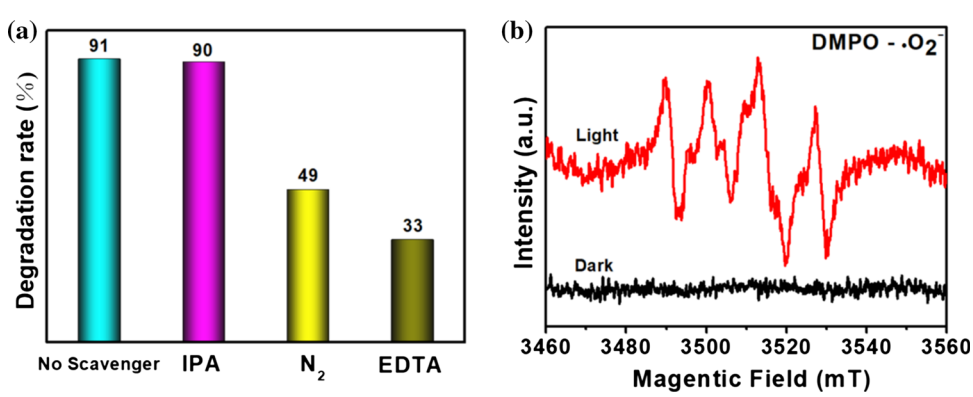

Figure 10 **a** Photocatalytic activities of ZSO@CN for the degradation of TC in the presence of different scavengers. **b** DMPO spin-trapping ESR spectrum for ZSO@CN (1:3) in methanol dispersion for capturing the signals of DMPO-•O_2^-.

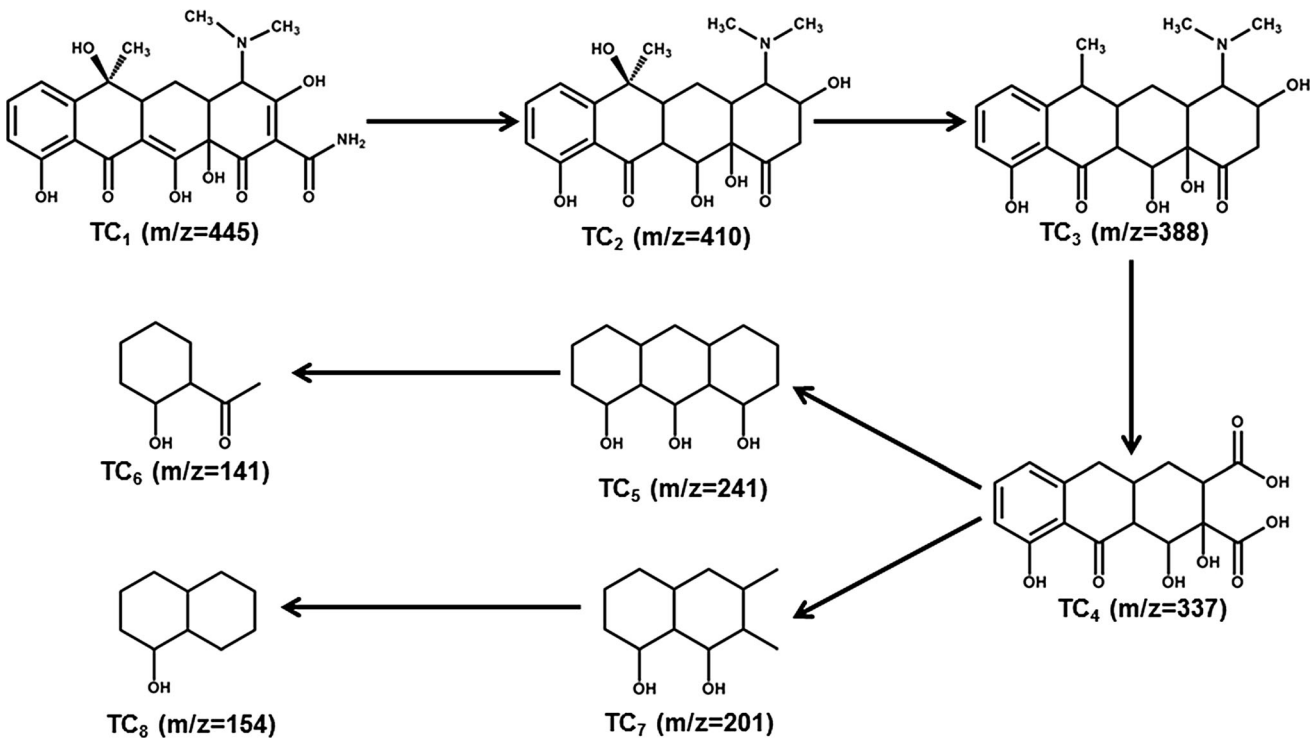

Figure 11 Possible TC degradation pathway of ZSO@CN core–shell photocatalyst.

pathways are revealed in Fig. 11, through further consideration of intermediates. Based on previous reports [50, 51], three typical functional groups (phenolic group, double bond and amine group) were easily attacked by O_2^- and h^+ [52, 53]. TC2 was formed through breaking bond reaction from TC. TC3 and TC4 were formed via dehydration reaction, losing N-methyl and ring opening reaction. The products TC5, TC6, TC7 and TC8 with smaller molecular weight were formed by ring opening reaction and the breaking bond reaction. The above reaction is actually produced by the synergistic effect of O_2^- and h^+. Finally, most of the intermediate products would be degraded into CO_2 and H_2O.

According to the above analysis, the possible photocatalytic mechanism over ZSO@CN core–shell heterostructure photocatalyst was initially described and is discussed in Fig. 12. By comparing the energy levels of ZSO with CN, it is exactly right to find that the energy levels of ZSO and CN are well-matched overlapping band structures for forming the type II heterojunction [46]. When exposed to visible light, due to the narrower band gap of CN (2.73 eV), the photoinduced electrons and holes were produced, while for ZSO (E_g = 3.25 eV), it was difficult to produce photogenerated charges during the visible light due to its broader band gap. The suitable energy band positions of CN and ZSO were inferred and are drawn in the right of Fig. 12. Specifically, the photoexcited electrons could transfer from CB of CN (− 1.16 eV vs. NHE) to the CB of ZSO (− 0.15 eV vs. NHE) and left the photoinduced holes on the VB of CN; hence, the separation rate of photogenerated electron–hole pairs was promoted effectively. The CB potential of ZSO was more negative than $O_2/\cdot O_2^-$ (− 0.046 eV vs. NHE); photogenerated electrons on the CB of ZSO can capture O_2 to form $\cdot O_2^-$ directly [54]. Owing to the VB of $\cdot OH/OH^-$ (2.38 eV vs. NHE) was higher CN (1.53 eV vs. NHE), therefore the h^+ directly oxidizes TC in VB of CN through photocatalytic reaction. At the same time, the process can be described as follows:

$$CN + hv \rightarrow CN\left(e^- + h^+\right) \quad (1)$$

$$CN\left(e^- + h^+\right) + ZSO \rightarrow CN\left(h^+\right) + ZSO\left(e^-\right) \quad (2)$$

$$ZSO\left(e^-\right) + O_2 \rightarrow {}^{\cdot}O_2^- \quad (3)$$

$${}^{\cdot}O_2^- + h^+ + TC \rightarrow CO_2 + H_2O \quad (4)$$

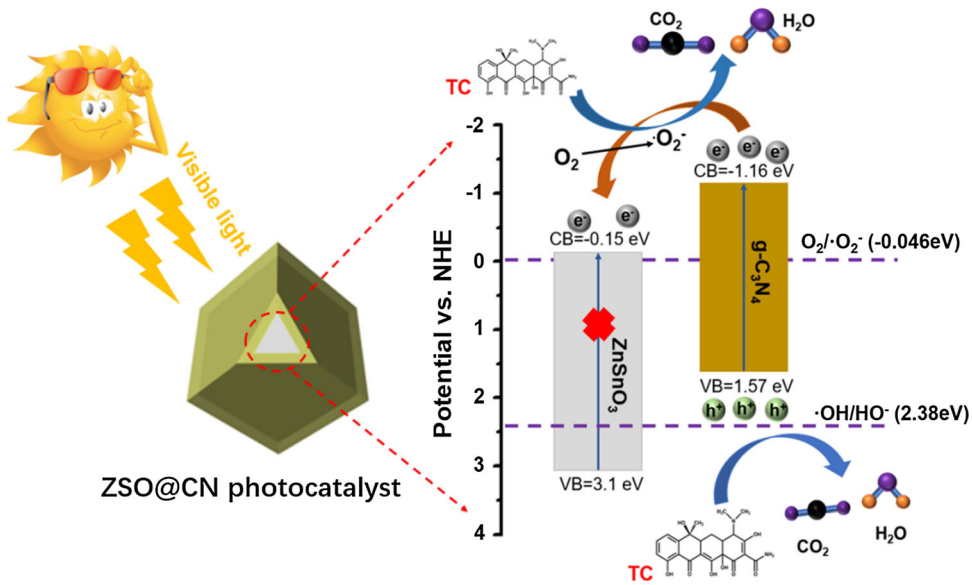

Figure 12 Proposed possible photocatalytic degradation mechanism of TC over ZSO@CN core–shell heterostructure photocatalyst.

Conclusions

In summary, ZSO@CN core–shell heterojunction was successfully constructed via a simple calcination route to improve the photocatalytic performance for the degradation of TC under visible light irradiation. The results indicated that the photocatalytic activity of as-prepared face-contact core–shell ZSO@CN is higher than that of pure ZSO, CN and point-contact ZSO-CN. The reason for higher photocatalytic degradation performance of face-contact ZSO-CN composite photocatalyst is mainly ascribed to the core–shell structure between CN and ZSO, which could own much more contact interfaces than that of point-contact ZSO-CN photocatalyst that play the part of efficient channels for charge transfer, leading to the higher photocatalytic degradation performance of face-contact ZSO-CN composite photocatalyst. The capture experiments indicated that both $\cdot O_2^-$ and h^+ played significant roles in the photocatalysis. This study laid a foundation to prepare for more ZSO-containing composite photocatalysts and promote the purification of wastewater containing organic pollutants.

Acknowledgement

This study is supported by the National Natural Science Foundations of China (No. 21906072 and No. 22006057), the Natural Science Foundation of Jiangsu Province (BK20190982), "Doctor of Mass entrepreneurship and innovation" Project in Jiangsu Province, and Doctoral Scientific Research Foundation of Jiangsu University of Science and Technology (China) (1062931806 and 1142931803).

Electronic supplementary material: The online version of this article (https://doi.org/10.1007/s10853-020-05542-1) contains supplementary material, which is available to authorized users.

References

[1] Gothwal R, Shashidhar T (2015) Antibiotic pollution in the environment: A review. Clean-Soil, Air, Water 43:479–489

[2] Guo F, Shi W, Li M, Shi Y, Wen H (2019) 2D/2D Z-scheme heterojunction of $CuInS_2$/g-C_3N_4 for enhanced visible-light-driven photocatalytic activity towards the degradation of tetracycline. Sep Purif Technol 210:608–615

[3] Guo F, Li M, Ren H, Huang X, Hou W, Wang C, Shi W, Lu C (2019) Fabrication of p-n $CuBi_2O_4/MoS_2$ heterojunction with nanosheets-on-microrods structure for enhanced photocatalytic activity towards tetracycline degradation. Appl Surf Sci 491:88–94

[4] Lu CY, Guo F, Yan QZ, Zhang ZJ, Li D, Wang LP, Zhou YH (2019) Hydrothermal synthesis of type II $ZnIn_2S_4/BiPO_4$ heterojunction photocatalyst with dandelion-like microflower structure for enhanced photocatalytic degradation of tetracycline under simulated solar light. J Alloy Compd 811:151976–151986

[5] Zhu Q, Sun Y, Na F, Wei J, Xu S, Li Y, Guo F (2019) Fabrication of CdS/titanium-oxo-cluster nanocomposites based on a Ti_{32} framework with enhanced photocatalytic activity for tetracycline hydrochloride degradation under visible light. Appl Catal B: Environ 254:541–550

[6] Shi W, Li M, Ren H, Guo F, Huang X, Shi Y, Tang Y (2019) Construction of a 0D/1D composite based on Au nanoparticles/$CuBi_2O_4$ microrods for efficient visible-light-driven photocatalytic activity. Beilstein J Nanotechnol 10:1360–1367

[7] Shi W, Li M, Huang X, Ren H, Guo F, Yan C (2020) Three-dimensional Z-Scheme $Ag_3PO_4/Co_3(PO_4)_2$@Ag heterojunction for improved visible-light photocatalytic degradation activity of tetracycline. J Alloy Compd 818:152883–152893

[8] Yang S, Liu C, Wang J, Lin X, Hong Y, Guo F, Shi J (2020) Enhanced photocatalytic activity of g-C3N4 quantum dots/$Bi_{3.64}Mo_{0.36}O_{6.55}$ nanospheres composites. J Solid State Chem 287:121347–121355

[9] Shi W, Liu C, Li M, Lin X, Guo F, Shi J (2020) Fabrication of ternary $Ag_3PO_4/Co_3(PO_4)_2/g\text{-}C_3N_4$ heterostructure with following Type II and Z-Scheme dual pathways for enhanced visible-light photocatalytic activity. J Hazard Mater 389:121907–121918

[10] Shi W, Li M, Huang X, Ren H, Guo F, Tang Y, Lu C (2020) Construction of $CuBi_2O_4/Bi_2MoO_6$ p-n heterojunction with nanosheets-on-microrods structure for improved photocatalytic activity towards broad-spectrum antibiotics degradation. Chem Eng J 394:125009–125019

[11] Jia MY, Yang ZH, Xu HY, Song PP, Xiong WP, Cao J, Zhang YR, Xiang YP, Hu JH, Zhou CY, Yang Y, Wang WJ (2020) Integrating N and F co-doped TiO_2 nanotubes with ZIF-8 as photoelectrode for enhanced photo-electrocatalytic degradation of sulfamethazine. Chem Eng J 388:124388–124401

[12] Wang C, Xu B-Q, Wang X, Zhao J (2005) Preparation and photocatalytic activity of $ZnO/TiO_2/SnO_2$ mixture. J Solid State Chem 178:3500–3506

[13] Chen L, Zhang Q, Huang R, Yin SF, Au CT (2012) Porous peanut-like Bi_2O_3-$BiVO_4$ composites with heterojunctions: one-step synthesis and their photocatalytic properties. Dalton Trans 41:9513–9518

[14] Borhade AV, Baste YR (2017) Study of photocatalytic asset of the $ZnSnO_3$ synthesized by green chemistry. Arab J Chem 10:S404–S411

[15] Guo F, Sun H, Cheng L, Shi W (2020) Oxygen-defective ZnO porous nanosheets modified by carbon dots to improve their visible-light photocatalytic activity and gain mechanistic insight. New J Chem 44:11215–11223

[16] Guo F, Huang X, Chen Z, Ren H, Li M, Chen L (2020) MoS_2 nanosheets anchored on porous ZnSnO3 cubes as an efficient visible-light-driven composite photocatalyst for the degradation of tetracycline and mechanism insight. J Hazard Mater 390:122158–122170

[17] Bing Y, Zeng Y, Liu C, Qiao L, Sui Y, Zou B, Zheng W, Zou G (2014) Assembly of hierarchical $ZnSnO_3$ hollow microspheres from ultra-thin nanorods and the enhanced ethanol-sensing performances. Sensors Actuat B: Chem 190:370–377

[18] Guo F, Huang X, Chen Z, Sun H, Shi W (2020) Investigation of visible-light-driven photocatalytic tetracycline degradation via carbon dots modified porous $ZnSnO_3$ cubes: Mechanism and degradation pathway. Sep Purif Technol 253:117518–117528

[19] Huang J, Xu X, Gu C, Wang W, Liu J (2012) Size-controlled synthesis of porous $ZnSnO_3$ cubes and their gas-sensing and photocatalysis properties. Sensors Actuat B: Chem 171–172:572–579

[20] Guo R, Tian R, Shi D, Li H, Liu H (2019) S-Doped $ZnSnO_3$ Nanoparticles with narrow band gaps for photocatalytic wastewater treatment. ACS Appl Nano Mater 2:7755–7765

[21] Shi W, Shu K, Huang X, Ren H, Li M, Chen F, Guo F (2020) Enhancement of visible-light photocatalytic degradation performance over nitrogen-deficient $g\text{-}C_3N_4/KNbO_3$ heterojunction photocatalyst. J Chem Technol Biotechnol 95:1476–1486

[22] Liu Y, Yang ZH, Song PP, Xu R, Wang H (2018) Facile synthesis of $Bi_2MoO_6/ZnSnO_3$ heterojunction with enhanced visible light photocatalytic degradation of methylene blue. Appl Surf Sci 430:561–570

[23] Lin L, Yu Z, Wang X (2019) Crystalline carbon nitride semiconductors for photocatalytic water splitting. Angew Chem Int Ed 58:6164–6175

[24] Shi W, Ren H, Huang X, Li M, Tang Y, Guo F (2020) Low cost red mud modified graphitic carbon nitride for the removal of organic pollutants in wastewater by the synergistic effect of adsorption and photocatalysis. Sep Purif Technol 237:116477–116485

[25] Sun H, Guo F, Pan J, Huang W, Wang K, Shi W (2021) One-pot thermal polymerization route to prepare N-deficient modified g-C3N4 for the degradation of tetracycline by the synergistic effect of photocatalysis and persulfate-based advanced oxidation process. Chem Eng J 406:126844–126856

[26] Murugesan P, Moses JA, Anandharamakrishnan C (2019) Photocatalytic disinfection efficiency of 2D structure graphitic carbon nitride-based nanocomposites: a review. J Mater Sci 54:12206–12235. https://doi.org/10.1007/s10853-019-03695-2

[27] Mousavi M, Hamzehloo M, Ghasemi JB (2020) Deposited $CuBi_2O_4$ and Bi_3ClO_4 nanoparticles on g-C3N4 nanosheet: a promising visible light-induced photocatalyst toward the removal of tetracycline hydrochloride and rhodamine B. J Mater Sci 55:7775–7791. https://doi.org/10.1007/s10853-020-04573-y

[28] Tan YG, Shu Z, Zhou J, Li TT, Wang WB, Zhao ZL (2018a) One-step synthesis of nanostructured g-C_3N_4/TiO_2 composite for highly enhanced visible-light photocatalytic H_2 evolution. Appl Catal B Environ 230:260–268

[29] Lv H, Ji G, Yang Z, Liu Y, Zhang X, Liu W, Zhang H (2015) Enhancement photocatalytic activity of the graphite-like C_3N_4 coated hollow pencil-like ZnO. J Colloid Interface Sci 450:381–387

[30] Zhang Q, Xu B, Yuan S, Zhang M, Ohno T (2017) Improving g-C_3N_4 photocatalytic performance by hybridizing with $Bi_2O_2CO_3$ nanosheets. Catal Today 284:27–36

[31] Huang X, Guo F, Li M, Ren H, Shi Y, Chen L (2020) Hydrothermal synthesis of $ZnSnO_3$ nanoparticles decorated on g-C_3N_4 nanosheets for accelerated photocatalytic degradation of tetracycline under the visible-light irradiation. Sep Purif Technol 230:115854

[32] Jin Y, Jiang D, Li D, Chen M (2017) Construction of ultrafine TiO_2 nanoparticle and $SnNb_2O_6$ nanosheet 0D/2D heterojunctions with abundant interfaces and significantly improved photocatalytic activity. Catal Sci Technol 7:2308–2317

[33] Hou H, Wang L, Gao F, Yang X, Yang W (2019) $BiVO_4$@TiO_2 core–shell hybrid mesoporous nanofibers towards efficient visible-light-driven photocatalytic hydrogen production. J Mater Chem C 7:7858–7864

[34] Liu J, Zhang G (2014) Ion-exchange synthesis of one-dimensional $Cd_2Ge_2O_6$/CdS core–shell composites and their enhanced visible-light photocatalytic activity. Appl Surf Sci 319:291–297

[35] An WJ, Sun KL, Hu JS, Cui WQ, Liu L (2020) The Z-scheme Ag_2CO_3@g-C_3N_4 core-shell structure for increased photoinduced charge separation and stable photocatalytic degradation. Appl Surf Sci 504:114345–114355

[36] Jia H, Roa R, Angioletti-Uberti S, Henzler K, Ott A, Lin X, Möser J, Kochovski Z, Schnegg A, Dzubiella J, Ballauff M, Lu Y (2016) Thermosensitive Cu_2O–PNIPAM core–shell nanoreactors with tunable photocatalytic activity. J Mater Chem A 4:9677–9684

[37] Lo M-K, Lee S-Y, Chang K-S (2015) Study of $ZnSnO_3$-nanowire piezophotocatalyst using two-step hydrothermal synthesis. J Phys Chem C 119:5218–5224

[38] Tang L, Feng C, Deng Y, Zeng G, Wang J, Liu Y, Feng H, Wang J (2018) Enhanced photocatalytic activity of ternary Ag/g-C_3N_4/$NaTaO_3$ photocatalysts under wide spectrum light radiation: The high potential band protection mechanism. Appl Catal B: Environ 230:102–114

[39] Mu Haq Z, Zhang XC, Rahman N, Khan S, Khatoon R, Hassan SS, Ye Z, Zhu L (2019) A two-step synthesis of microsphere-decorated fibers based on NiO/$ZnSnO_3$ composites towards superior ethanol sensitivity performance. J Alloy Compd 777:73–83

[40] Wang Y, Yang W, Chen X, Wang J, Zhu Y (2018) Photocatalytic activity enhancement of core-shell structure g-C_3N_4@TiO_2 via controlled ultrathin g-C_3N_4 layer. Appl Catal B: Environ 220:337–347

[41] Wang J, Huang J, Xie H, Qu A (2014) Synthesis of g-C_3N_4/TiO_2 with enhanced photocatalytic activity for H_2 evolution by a simple method. Int J Hydrogen Energ 39:6354–6363

[42] Tan Y, Shu Z, Zhou J, Li T, Wang W, Zhao Z (2018b) One-step synthesis of nanostructured g-C_3N_4/TiO_2 composite for highly enhanced visible-light photocatalytic H_2 evolution. Appl Catal B: Environ 230:260–268

[43] Park H, Park TJ, Huh YS, Choi BG, Ko S, Lee SY, Hong WH (2010) Immobilization of genetically engineered fusion proteins on gold-decorated carbon nanotube hybrid films for the fabrication of biosensor platforms. J Colloid Interface Sci 350:453–458

[44] Yang YH, Li XL, Lu C, Huang WH (2019) G-C_3N_4 Nanosheets Coupled with TiO_2 Nanosheets as 2D/2D heterojunction photocatalysts toward high photocatalytic activity for hydrogen production. Catal Lett 149:2930–2939

[45] Yuvaraj S, Amaresh S, Lee YS, Selvan RK (2014) Effect of carbon coating on the electrochemical properties of Co_2SnO_4 for negative electrodes in Li-ion batteries. RSC Adv 4:6407–6416

[46] Shi W, Shu K, Sun H, Ren H, Li M, Chen F, Guo F (2020) Dual enhancement of capturing photogenerated electrons by loading CoP nanoparticles on N-deficient graphitic carbon nitride for efficient photocatalytic degradation of tetracycline under visible light. Sep Purif Technol 246:116930-116939

[47] Yuan YJ, Shen ZK, Wu ST, Su YB, Pei L, Ji ZG, Ding MY, Bai WF, Chen YF, Yu ZT, Zou ZG (2019) Liquid exfoliation of g-C_3N_4 nanosheets to construct 2D–2D MoS_2/g-C_3N_4 photocatalyst for enhanced photocatalytic H_2 production activity. Appl Catal B: Environ 246:120–128

[48] Wang L, Jin P, Duan S, She H, Huang J, Wang Q (2019) In-situ incorporation of Copper(II) porphyrin functionalized zirconium MOF and TiO_2 for efficient photocatalytic CO_2 reduction. Sci Bull 64:926–933

[49] Barhoumi N, Olvera-Vargas H, Oturan N, Huguenot D, Gadri A, Ammar S, Brillas E, Oturan MA (2017) Kinetics of oxidative degradation/mineralization pathways of the antibiotic tetracycline by the novel heterogeneous electro-

Fenton process with solid catalyst chalcopyrite. Appl Catal B: Environ 209:637–647

[50] Deng F, Zhao L, Luo X, Luo S, Dionysiou DD (2018) Highly efficient visible-light photocatalytic performance of $Ag/AgIn_5S_8$ for degradation of tetracycline hydrochloride and treatment of real pharmaceutical industry wastewater. Chem Eng J 333:423–433

[51] Zhao S, Chen J, Liu Y, Jiang Y, Jiang C, Yin Z, Xiao Y, Cao S (2019) Silver nanoparticles confined in shell-in-shell hollow TiO_2 manifesting efficiently photocatalytic activity and stability. Chem Eng J 367:249–259

[52] Xie ZJ, Feng YP, Wang FL, Chen DN, Zhang QX, Zeng YQ, Lv WY, Liu GG (2018) Construction of carbon dots modified MoO_3/g-C_3N_4 Z-scheme photocatalyst with enhanced visible-light photocatalytic activity for the degradation of tetracycline. Appl Catal B: Environ 229:96–104

[53] Wang DD, Li J, Xu ZF, Zhu YR, Chen GX, Cui Z (2019) Synthesis of g-C_3N_4/NiO p-n heterojunction materials with ball-flower morphology and enhanced photocatalytic performance for the removal of tetracycline and Cr^{6+}. J Mater Sci 54:11417–11434

[54] Sheng Y, Wei Z, Miao H, Yao W, Li H, Zhu Y (2019) Enhanced organic pollutant photodegradation via adsorption/photocatalysis synergy using a 3D g-C_3N_4/TiO_2 free-separation photocatalyst. Chem Eng J 370:287–294